Model-Based Studies of Eddy Current Sensors for the Characterization of Corrosion under Coatings

Daniel Bartles[1], Eric Tarkleson[1], Prof. Mahmoodul Haq[1], Prof. Lalita Udpa[1], Dr. Tom Sanders[2]

[1]Non-Destructive Evaluation Laboratory
Michigan State University
East Lansing, Michigan 48824

[2]U.S. Army CCDC Ground Vehicle Systems Center
Materials – Environmental, Coatings & Corrosion (MECC)
FCDD-GVS-ES, MS 268A

ABSTRACT

Steel and aluminum infrastructures can corrode when exposed to harsh environmental conditions, such as extreme moisture or temperature. Consequently, these structures are coated with protective layers in an effort to reduce corrosion damage. However, when corrosion is hidden by paint or coatings with certain electrical and magnetic properties, the damage can be detected visually only after the paint blisters, which occurs after the corrosion damage is severe. Hence, there is a need for developing nondestructive evaluation (NDE) methods for early detection and quantification of corrosion under coatings. This paper investigates the development of an eddy current sensor array system for early detection and quantification of corrosion under coating in steel and aluminum samples. The feasibility and effectiveness of the approach is investigated using a combination of model-based and experimental data.

A validated numerical model is used to predict the probe response to corrosion defects concealed beneath a layer of paint or other protective coating. In particular, we consider corrosion damage with arbitrary electromagnetic material properties – e.g. electric conductivity, magnetic permeability. A radial basis function neural network (RBFNN) is designed to read in the probe signal and estimate the depth profile of corrosion. Simulation results after calibration, are used for training the RBFNN to determine the map from signal space to defect space.

Keywords: eddy current, corrosion under paint, FEM, radial basis function, neural network

Introduction

Nature relentlessly opposes our aspirations to construct durable and enduring structures. Metal structures naturally corrode over time due to the conditions of their environment, and certain conditions have been shown to accelerate corrosion. Corrosion can progress in various ways, but among the most serious is pitting corrosion. Initial pit formation is small and can go undetected. Once a pit develops, it can be self-sustaining and self-propagating, causing serious damage before being detected. Organic coatings are a common method of protection against the corrosion of metal structures. Due to their composition, they may be conductive or perhaps magnetic, complicating early pit detection.

This paper presents the development of eddy current NDE sensors and systems for the detection and characterization of corrosion damage under paint/coating. There are a wide variety of organic coatings available and it is important to understand the effect this will have on the signal response of an eddy current probe measurement, since the signal due to pitting corrosion is already small. In order to investigate such effects and optimize the sensor design, a finite-element model (FEM) was developed to simulate eddy current inspection and predict signals due to arbitrary defects in a sample, under a variety of experimental conditions. The model was validated using a calibration sample with machined defects, and simulations were conducted to study the effect of coatings with

various electromagnetic properties, on the probe signal The FEM signals were also used to train and test radial basis function neural networks (RBFNN) that were used to estimate the corrosion depth profiles based on simulated and experimental signals.

Eddy Current Testing

Eddy current testing (ECT) is the most commonly used electromagnetic nondestructive examination technique that is used to inspect a conductive sample. In ECT, an alternating current is passed through a probe coil which induces eddy currents in the conductive sample, when the probe is scanning the sample surface. The induced field associated with eddy currents affects the impedance of the probe. As the probe scans the sample surface, defects in the sample will perturb the eddy currents, which will change the probe impedance. The changes in the probe's impedance can be analyzed for information about the defect depth and shape (defect profile). In this paper, a single absolute coil is considered in the finite element modeling studies of the problem.

Finite-Element Modeling (A-V formulation)

Finite-element modeling (FEM) is a useful tool for solving forward problems in physics and engineering. In general, the FE model solves the partial differential equation governing the underlying physics. The governing equation for eddy current NDE is derived from Maxwell's equations in the quasi-stationary limit as [1].

$$\nabla \times \boldsymbol{H} = \boldsymbol{J} \qquad \text{(Eq. 1)}$$

$$\nabla \times \boldsymbol{E} = -\frac{\partial \boldsymbol{B}}{\partial t} \qquad \text{(Eq. 2)}$$

$$\nabla \cdot \boldsymbol{B} = 0 \qquad \text{(Eq. 3)}$$

where
H is the magnetic field strength,
J is the current density,
E is the electric field strength,
B is the magnetic flux density.

The constitutive relationships are given by

$$\boldsymbol{H} = \nu \boldsymbol{B} \qquad \text{(Eq. 4)}$$

$$\boldsymbol{J} = \sigma \boldsymbol{E} \qquad \text{(Eq. 5)}$$

where
ν is the reluctivity, and
σ is the conductivity.

The test geometry can be divided into the two regions depicted in Figure 1: Ω_1 and Ω_2, where $\Omega = \Omega_1 \cup \Omega_2$. Region Ω_1 is the conductor and contains the eddy currents induced by the source field due to the coil present in the surrounding air, denoted as region Ω_2.

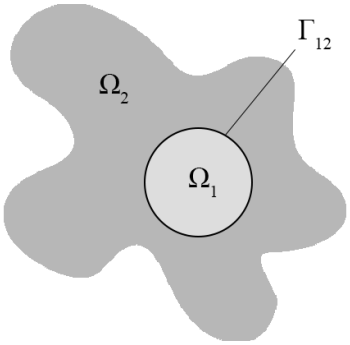

Figure 1: Schematic of test geometry with different regions and boundaries

The interface between regions 1 and 2 is denoted Γ_{12}, and the interface conditions on this boundary are given by

$$\boldsymbol{B_1} \cdot \boldsymbol{n_1} + \boldsymbol{B_2} \cdot \boldsymbol{n_2} = 0 \qquad \text{(Eq. 6)}$$

$$\boldsymbol{H_1} \times \boldsymbol{n_1} + \boldsymbol{H_2} \times \boldsymbol{n_2} = 0 \qquad \text{(Eq. 7)}$$

where **n** is the unit vector normal to the corresponding surface.

The **A**-V formulation uses the magnetic vector potential **A** related to the magnetic flux density by $\boldsymbol{B} = \nabla \times \boldsymbol{A}$ in Equations 1 and 2, which results in the governing equations[1].

$$\nabla \times v\nabla \times \boldsymbol{A} + \sigma \frac{\partial \boldsymbol{A}}{\partial t} + \sigma \nabla \mathrm{V} = \boldsymbol{0} \qquad \text{in } \Omega_1 \qquad \text{(Eq. 8)}$$

$$\nabla \times v\nabla \times \boldsymbol{A} = \boldsymbol{J}_s \qquad \text{in } \Omega_2 \qquad \text{(Eq. 9)}$$

where
$\boldsymbol{A}$ is the vector potential,
V is the scalar potential, and
$\boldsymbol{J}_s$ is the source current density.

The FE model solves for the nodal values of 3 components of **A** and scalar value of V. The probe impedance is calculated from **A** after post processing [1], [2].

Model Validation

In order to validate the FE model, a calibration steel plate with dimensions 30 mm length, 30 mm width and 6 mm thickness with 9 flat-bottom-hole defects of known diameter and depth was fabricated as seen in Figure 2.

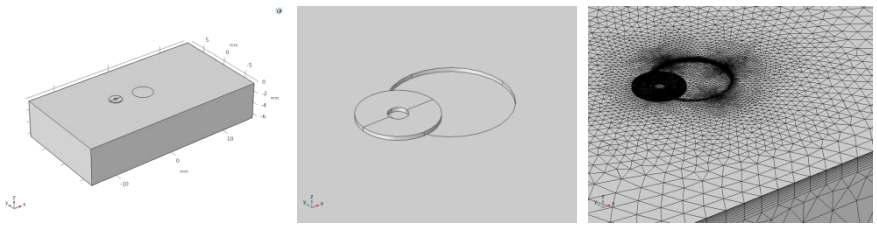

(a) **(b)** **(c)**

Figure 2: (a) The model geometry with sample, defect, coil, (b) defect-coil geometry (zoomed in), (c) finite-element mesh

The geometry of the nine machined defects are summarized in Table 1.

Plate Properties: Electrical conductivity (S/m) = 6.0e+06; Relative permeability (μ_r) = 100		
Defect:	**Diameter: mm (in)**	**Depth: mm (in)**
1	1.587mm (0.0625in)	0.3175mm (0.0125in)
2	1.587mm (0.0625in)	0.6350mm (0.0250in)
3	1.587mm (0.0625in)	1.2700mm (0.0500in)
4	3.175mm (0.1250in)	0.3175mm (0.0125in)
5	3.175mm (0.1250in)	0.6350mm (0.0250in)
6	3.175mm (0.1250in)	1.2700mm (0.0500in)
7	6.350mm (0.2500in)	0.3175mm (0.0125in)
8	6.350mm (0.2500in)	0.6350mm (0.0250in)
9	6.350mm (0.2500in)	1.2700mm (0.0500in)

Table 1: Details of defects machined on calibration plate

The model predicted signals were calibrated using experimental measurements from one flaw (#8) and the calibrated signals were compared with experimental signals from other flaws. The results, for the imaginary parts of the signals are presented in Figure 3, showing a comparison between experimental signals and calibrated model predictions which validate the model performance. The three signals shown in Figure 3 correspond to defects #7 (blue), #8 (red), and #9 (green), as listed in Table 1.

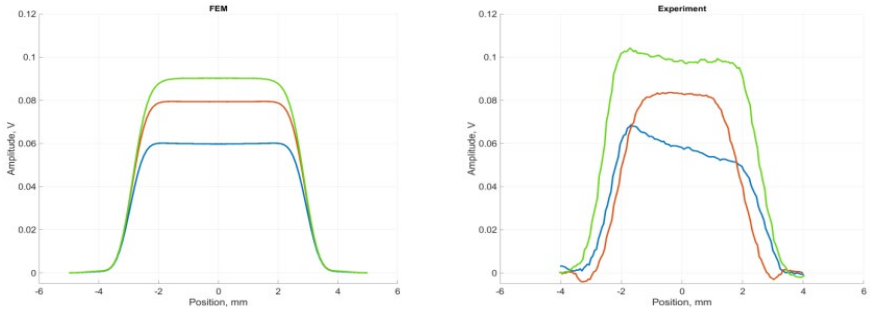

(a) **(b)**

Figure 3: Imaginary parts of the simulated signals after scaling (a) and experimental signals (b) for the machined calibration plate defects

Model-Based Parametric Studies

The validated model was used to study eddy current signals under different conditions. Factors known to influence the eddy current signal are:

- Electrical conductivity of the specimen
- Magnetic permeability of the specimen
- Size of discontinuities, such as cracks, corrosion, pitting

The effects of these parameters were studied by conducting model-based parametric studies. The parameters studied and the ranges of values considered are summarized in Table 2.

Parameter Values for Model-Based Studies	
Defect Diameter (mm [in])	1.587 [0.0625], 3.175 [0.125], 6.350 [0.25]
Defect Depth (mm)	0.1, 0.2, 0.3, 0.4, 0.5, 0.6, 0.7, 0.8
Coating Conductivity (S/m)	1e0, 1e6, 6e6
Coating Permeability	1, 10, 100
Coating Thickness (mm)	0.1, 0.5

Table 2: Parametric study variable values

The results of these parametric studies are presented in the following Figure 4 - Figure 7.

Figure 4 shows the signal response to parametric variations of defect depth and diameter. As expected, the signal magnitude increases nonlinearly with defect size due to skin effect phenomenon. These signals are also used to train the neural networks.

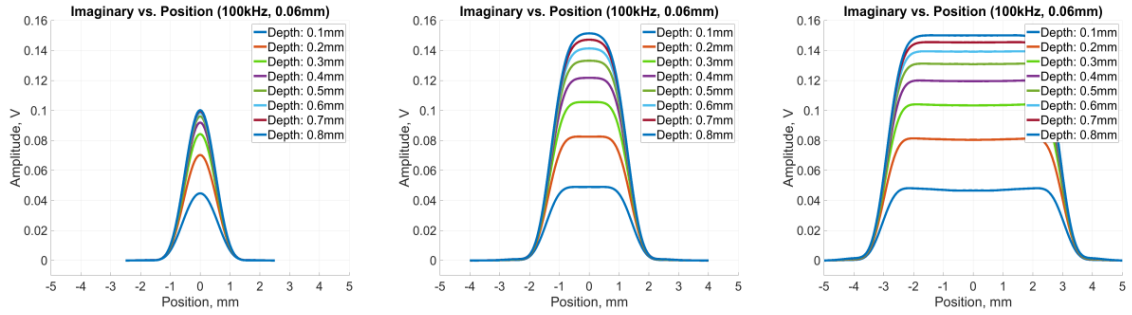

(a) **(b)** **(c)**

Figure 4: Signal response due to changes in defect depth and diameter; (a) 1.587mm diameter defect, (b) 3.175mm diameter defect, (c) 6.35mm diameter defect. The depths are varied from 0.1mm through 0.8mm in 0.1mm increments.

Figure 5 shows the signal response due to changes in the coating's conductivity. Here, a signal enhancement can be seen in the response for highly-conductive coatings. The induced current in the defect region is proportional to the coating conductivity, resulting in enhanced signal amplitude.

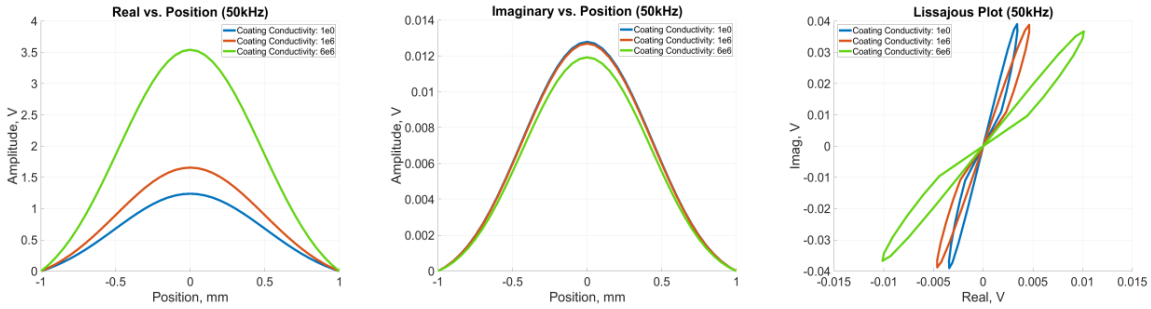

(a) **(b)** **(c)**

Figure 5: Signal response due to changes in coating conductivity; (a) real signal, (b) imaginary signal, and (c) Lissajous plots. The blue curve is due to nonconductive (1e0 S/m) coating, Red curve is from slightly-conductive coating (1e6 S/m) coating, and the green curve is from highly-conductive coating (6e6 S/m)

Parametric studies of coating thickness were carried out next for highly-conductive coatings and the results are presented in Figure 6. Although the signal amplitude is enhanced for thin coatings, simulation results correctly show that signal amplitude decreases with coating thicknesses greater than 0.5mm, due to skin effect.

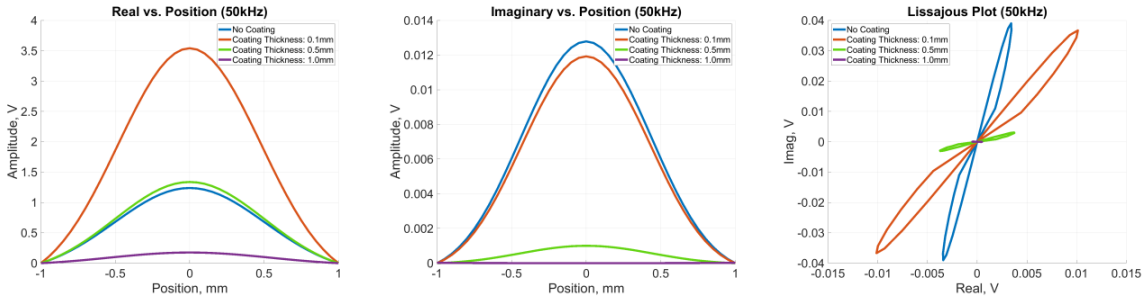

(a) **(b)** **(c)**

Figure 6: Signal response of highly-conductive coatings (6e6S/m) due to changes in coating thickness; (a) real signal, (b) imaginary signal, and (c) Lissajous plot. (Blue) - no coating (Red) - 0.1mm thickness, (Green)- 0.5mm thickness and (Purple) -1.0mm thickness

Parametric studies of coating permeability were considered next, and the results are displayed in Figure 7. In contrast to the coating conductivity studies, signal strength was observed to be inversely proportional to coating permeability. A reduction in induced current density in the defect region was observed. This was due to the channeling of magnetic flux lines within the coating, which then do not induce eddy currents near the defect beneath the coating.

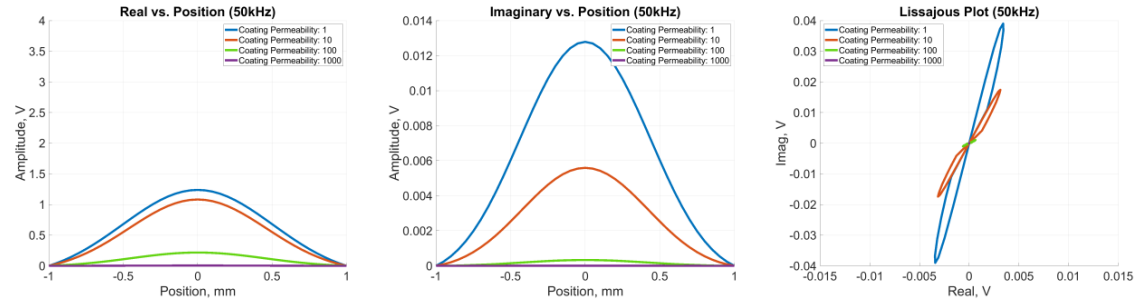

(a) **(b)** **(c)**

Figure 7: Simulation results for different values of coating permeability; (a) real signal, (b) imaginary signal, and (c) Lissajous plots. Blue - ($\mu_r = 1$), Red - ($\mu_r = 10$), Green - ($\mu_r = 100$) , Purple - ($\mu_r = 1000$)

Radial Basis Function Neural Networks

A second objective of this paper is to analyze the probe measurements in terms of corrosion depth. Neural networks have proven to be a powerful tool for a wide variety of applications, from image recognition to defect characterization. In this case, a neural network which predicts the defect depth profile corresponding to an eddy current signal is desired. The radial basis function neural network illustrated Figure 8, has been well documented in literature [3].

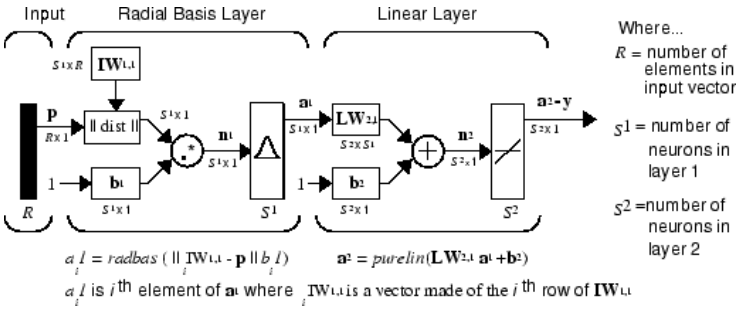

Figure 8: Radial Basis Function Neural Network Schematic [4]

The mathematical operation performed by the neuron depends on the activation function. In the case of a radial basis neural network, the activation function is a radially symmetric basis function.

$$\boldsymbol{n} = \boldsymbol{b} * \boldsymbol{f}(\|\bar{\boldsymbol{x}} - \bar{\boldsymbol{x}}_{\boldsymbol{i}}\|) \qquad \textbf{(Eq. 10)}$$

where
$\bar{\boldsymbol{x}}$ is an input vector
$\bar{\boldsymbol{x}}_{\boldsymbol{i}}$ are input weights or centers
$\boldsymbol{b}$ is parameter related to a Gaussian function

A neural network is put to use in two phases: training and testing. During training, a set of input data (signal) is fed into the input layer of the neural network along with known output data (known depth profiles), applied at output layer nodes. During training, the neural network "learns" by mathematically determining weights that link the input and output data. After the neural network has been trained, when an unknown test data (measured signal) is applied the network's output provides an estimate of the corresponding corrosion profile.

Simulated ECT signals were generated for circular flat-bottom defects of different depth and diameter as listed in Table 2 using the FE model. The partitioning of the signal-depth pairs are used into training and test data are described in Table 3. The signal vectors are complex-valued resulting in an $\boldsymbol{n}$-element complex vector corresponding to $\boldsymbol{n}$ locations in each scan.

Simulated Data for Training	
Depths:	0.1mm, 0.3mm, 0.5mm, 0.7mm, 0.8mm
Diameters:	1.587mm, 3.175mm, 6.35mm

Simulated Data for Testing	
Depths:	0.2mm, 0.4mm, 0.6mm
Diameters:	1.587mm, 3.175mm, 6.35mm

Table 3: Simulated data used for training and testing, respectively

The real and imaginary signals are then broken up into sub-vectors of three elements which are paired to the defect depth at the location corresponding to the center element in the vector, shown in Figure 9. An alternate 6-dimensional input vector can also be considered by concatenating three-element input vectors from real and imaginary parts of the signal as illustrated schematically Figure 10. This procedure can also be extended to create five-element input vectors and ten-element concatenated vectors. The neural network using 3-element input from the imaginary signals alone will be referred to as RBFNN1; the neural network using the concatenated real and imaginary vectors will be referred to as RBFNN2.

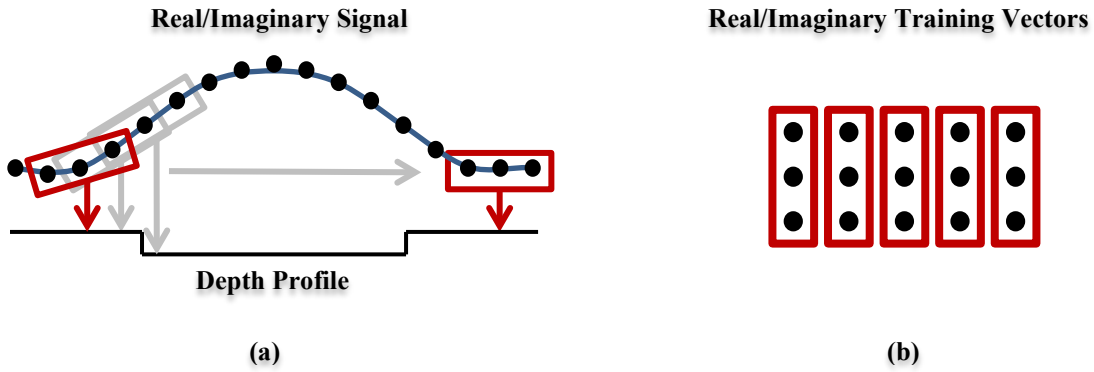

Figure 9: Input data generation for RBFNN1; (a) The real or imaginary part of the signal; (b) 3-element length input signal vectors derived from real/imaginary signal

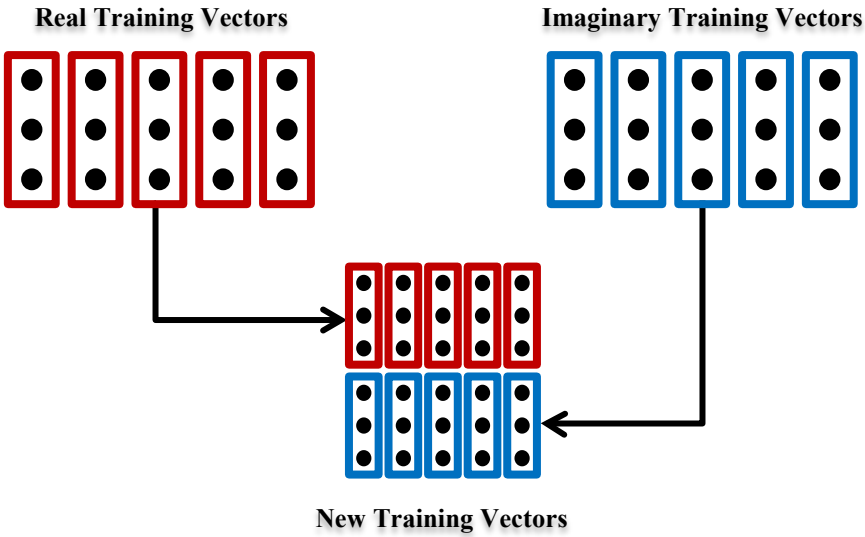

Figure 10: Input data generation for RBFNN1; real and imaginary input vectors are concatenated to produce 6-element length input vectors

Results – Simulation Data

Calibrated simulated data was used to train and test the neural network. The simulated data is separated into training and testing data sets, as described in Table 3. Both sets of data are processed into input matrices as described in Figure 9 and Figure 10. Defect profile vectors indicating the depth of the defect at every point in the scan are created and the signal-defect pairs are used to train the neural network. After the network is trained, the test data (see Table 3) is used to evaluate the network's performance. For each test signal input, the corresponding defect profile is computed.

Prediction results on training and testing data are shown in Table 4. To evaluate the performance of the different networks, the average predicted depth in the defect area, is compared with true depth – for RBFNN1 and RBFNN2 for both 5-element and 3-element networks. Overall, the 5-element neural networks have a lower average error than the 3-element neural networks, and the RBFNN2 has lower average error than RBFNN1 when tested on simulation data. This is as expected as the amount of information used is increased in the case of 5-element vectors.

Summary: Average Predicted Depth on Simulation Data with RBFNN												
True Depth:	Defect Diameter: 1.587mm				Defect Diameter: 3.175mm				Defect Diameter: 6.35mm			
	3-Element		5-Element		3-Element		5-Element		3-Element		5-Element	
	NN1	NN2	NN1	NN2	NN1	NN2	NN1	NN2	NN1	NN2	NN1	NN2
0.1mm	0.09	0.13	0.07	0.08	0.09	0.07	0.08	0.10	0.08	0.09	0.10	0.09
0.2mm	0.27	0.29	0.21	0.23	0.24	0.20	0.18	0.22	0.21	0.21	0.19	0.19
0.3mm	0.38	0.42	0.36	0.37	0.38	0.33	0.31	0.31	0.33	0.31	0.30	0.29
0.4mm	0.43	0.50	0.46	0.48	0.46	0.45	0.43	0.40	0.42	0.37	0.41	0.40
0.5mm	0.47	0.54	0.53	0.56	0.56	0.56	0.54	0.50	0.51	0.48	0.52	0.49
0.6mm	0.48	0.57	0.57	0.61	0.64	0.64	0.64	0.61	0.62	0.57	0.61	0.60
0.7mm	0.50	0.58	0.60	0.64	0.70	0.71	0.71	0.70	0.69	0.68	0.70	0.70
0.8mm	0.51	0.59	0.61	0.65	0.76	0.76	0.76	0.77	0.77	0.79	0.76	0.79

Table 4: Prediction Results on Training and Testing Data (FEM)

In Table 5 and Table 6, profile prediction results are shown graphically for the test defect of depth 0.2mm and 3 diameters as listed in Table 3. From these results, artifacts are observed near the sharp transitions of depth profile. These artifacts are particularly severe in the case of small diameter defects as seen in the 3-element RBFNN1 for DIA 1.587mm (Table 5). The error is reduced for 5-element neural networks (Table 6). Significant improvement is seen in the average predicted depth for small diameters.

3-Element RBFNN1 (IM) Results on Testing Data			
	DIA: 1.587mm	DIA: 3.175mm	DIA: 6.35mm
True Depth: 0.2mm	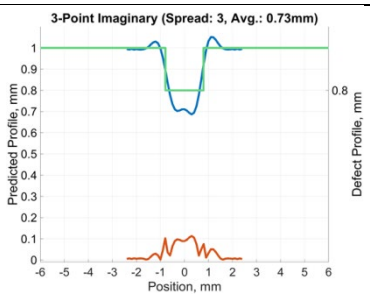	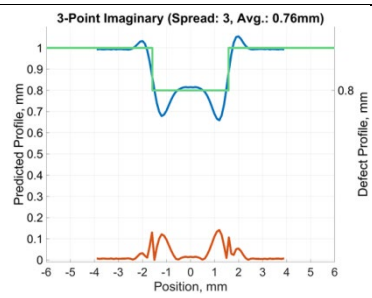	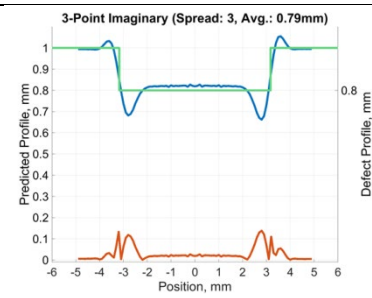
	Avg. Predicted Depth: 0.27	**Avg. Predicted Depth: 0.24**	**Avg. Predicted Depth: 0.21**

Table 5: 3-Element RBFNN1 Prediction Results on Test Data (FEM) - predicted profile (blue), true profile (green), and the absolute error (red)

5-Element RBFNN1 (IM) Results on Testing Data			
	DIA: 1.587mm	DIA: 3.175mm	DIA: 6.35mm
True Depth: 0.2mm	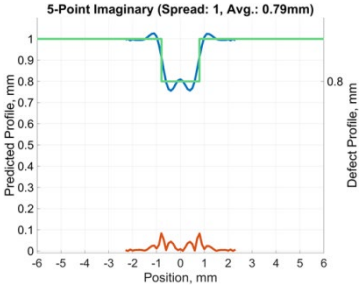	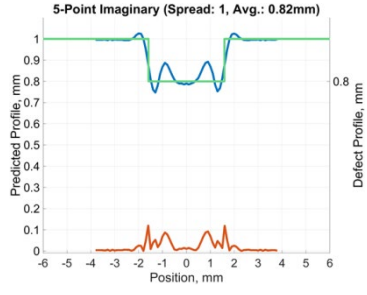	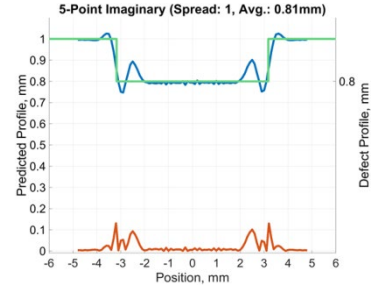
	Avg. Predicted Depth: 0.21	**Avg. Predicted Depth: 0.18**	**Avg. Predicted Depth: 0.19**

Table 6: 5-Element RBFNN1 Prediction Results on Test Data (FEM) - predicted profile (blue), true profile (green), and the absolute error (red)

Results – Experimental Data

RBFNN1 was also used to predict the depth of the calibration plate defects of depth 0.3175mm, and 3 different diameters, using experimental data. The true and predicted depths for different diameters are shown in Table 7.

Summary: Average Predicted Depth on Experimental Data with RBFNN1						
True Depth: (mm)	Defect Diameter: 1.587mm		Defect Diameter: 3.175mm		Defect Diameter: 6.35mm	
	3-Element NN1	5-Element NN1	3-Element NN1	5-Element NN1	3-Element NN1	5-Element NN1
0.3175	0.28	0.27	0.21	0.21	0.38	0.38

Table 7: Prediction Results on Experimental Data

Conclusion and Future Work

Eddy current testing has been shown to successfully small surface corrosion defects that are concealed under a coating in steel samples. A finite element model was developed and used to study the effect of various parameters such as electromagnetic property of the coating, on the probe signal from various defects. These parametric studies suggest that thin, conductive coatings can actually enhance the signal due to defects beneath the coating, due to increased current density in the defect region. On the contrary, magnetic coatings act to suppress the signal, due to their shielding effect which leads to decreased current density in the defect region. Depth estimation algorithms using RBFNN were also investigated. Initial results show that the RBFNN approach offers a simple solution for depth profile estimation. More extensive testing of the algorithm on a larger set of arbitrary defect profiles is progress. Work is also underway to study effect of different electromagnetic properties of corrosion materials and corrosion pitting geometries.

Acknowledgements

This work was supported by the U.S. Department of Defense NCMS under cooperative agreement award No. HQ0034-15-2-0007

We would also like to thank Mr. Jim Muns and Mr. Rob Bennett in the MSU PA Machine Shop for their help machining our calibration plate.

REFERENCES

[1] O. Biro and K. Preis, "On the Use of the Magnetic Vector Potential in the Finite Element Analysis of Three-Dimensional Eddy Currents," *IEEE Transactions on Magnetics Vol. 25 No. 4,* pp. 3145-3159, July 1989.

[2] L. Udpa and W. Lord, "Impedance and Mesh Structure Considerations in the Finite Element Analysis of Eddy Current NDT Probe Phenomena," *IEEE Transactions on Magnetics,* Vols. MAG-21, no. 6, pp. 2269-2272, 1985.

[3] P. Ramuhalli, L. Udpa and S. Udpa, "Electromagnetic NDE Signal Inversion by Function-Approximation Neural Networks," *IEEE Transactions on Magnetics,* vol. 38, no. 6, pp. 3633-3642, 2002.

[4] "Radial Basis Neural Networks - MATLAB & Simulink," [Online]. Available: https://www.mathworks.com/help/deeplearning/ug/radial-basis-neural-networks.html. [Accessed September 2019].